High performance oxide-based p-n heterojunctions integrating p-SnO_x and n-InGaZnO

Dong Hun Lee¹, Honghwi Park², Michael Clevenger¹, Hyeonghun Kim¹, Chung Soo Kim³, Mingyuan Liu¹, Giyong Kim⁴, Han Wook Song⁵, Kwangsoo No⁶, Sung Yeol Kim⁴, Dong-Kyun Ko⁷, Anne Lucietto¹, Hongsik Park², and Sunghwan Lee¹*

Keywords: p-type oxide; SnO_x; p-n junction; diode; heterojunction; InGaZnO (IGZO)

¹ School of Engineering Technology, Purdue University, West Lafayette, IN 47907, USA

² School of Electronic and Electrical Engineering, Kyungpook National University, Daegu 41566, Republic of Korea

³ Analysis Technical Center, Korea Institute of Ceramic Engineering and Technology, Jinju, Gyeongsangnam-do 52851, Republic of Korea

⁴ School of Mechanical Engineering, Kyungpook National University, Daegu 41566, Republic of Korea

⁵Center for Mass and Related Quantities, Korea Research Institute of Standard and Science, Daejeon 34113, Republic of Korea

⁶Department of Materials Science and Engineering, KAIST, Daejeon 34141, Republic of Korea

⁷ Department of Electrical and Computer Engineering, New Jersey Institute of Technology, Newark, NJ 07102, USA

^{*}Corresponding authors: sunghlee@purdue.edu

Abstract

The fabrication of oxide-based p-n heterojunctions that exhibit high rectification performance have been difficult to realize using standard manufacturing techniques that feature mild vacuum requirements, low thermal budget processing, and scalability. Critical bottlenecks in the fabrication of these heterojunctions include the narrow processing window of p-type oxides and the charge blocking performance across the metallurgical junction required for achieving low reverse current and hence high rectification behavior. The overarching goal of the present study is to demonstrate a simple processing route to fabricate oxide-based p-n heterojunctions that demonstrate high on/off rectification behavior, low saturation current, and a small turn-on voltage. For this study, room-temperature sputter-deposited p-SnO_x and n-InGaZnO (IGZO) films were chosen. SnO_x is a promising p-type oxide material due to its mono-cationic system that limits complexities related to processing and properties, compared to other multi-cationic oxide materials. For the n-type oxide, IGZO is selected due to the knowledge that postprocessing annealing critically reduces the defect and trap densities in IGZO to ensure minimal interfacial recombination and high charge blocking performance in the heterojunctions. The resulting oxide p-n heterojunction exhibits a high rectification ratio greater than 10^3 at ± 3 V, a low saturation current of $\sim 2 \times 10^{-10}$ A, and a small turn-on voltage of ~ 0.5 V. In addition, the demonstrated oxide p-n heterojunctions exhibit excellent stability over time in air due to the p-SnO_x with completed reaction annealing in air and the reduced trap density in n-IGZO.

1. Introduction

The discovery of high-mobility oxide semiconductors has sparked considerable research interest, leading to the development of electronic materials that are electrically and chemically stable, can be produced at mild temperatures (<500 °C), and can be manufactured at low costs. Of the many oxide semiconductors, most researchers have focused towards transition metal oxides¹⁻³ that incorporate In^{1,4-6}, Sn^{4,7-8}, Ga^{1,9-10}, Al¹¹⁻¹³ and Zn^{3,7-8,11,14}. These materials exhibit notably higher carrier mobility^{8, 15-18} (10-50 cm²/Vs) than conventional amorphous Si^{1, 16} (a-Si, <1 cm²/Vs), as well as the potential for low temperature manufacturing^{1, 6, 16, 19-21} (<200 °C). The high carrier mobility characteristics of these oxides indicate a strong potential for the replacement of a-Si in current displays, as these oxides are already being implemented in both active-matrix liquid crystal displays and organic light emitting diode technologies 16, 22-23. In spite of such a high mobility of oxide semiconductors, the oxides reported in the literature are mostly limited to single polarity, n-type, applications ^{1-4, 6, 15, 24}. This is due primarily to the reason that the current synthesis of p-type oxide semiconductors is technologically challenging²⁵⁻²⁶. As a result, current applications of oxide thin film transistors (TFTs) are only subject to n-type devices and have been limited to displays as pixel driving elements in which circuits are composed only of n-channel TFTs.

Due to the technical challenges, the reports on p-type oxides are quite limited. Strategies to produce p-type oxide semiconductors have been suggested²⁵⁻²⁶ based on the formation of hybrid orbitals²⁵⁻²⁶ in order to broaden the valence band in certain oxide systems. The hybrid orbitals provide delocalized oxygen 2p states or cation valence states at similar energy levels to the oxygen 2p states near the valence band maximum (VBM). Meng $et\ al.^{27}$ suggests that, oxygen 2p

orbitals in typical metal oxides are likely placed at deep level states and therefore strongly localized in the valence band, which inhibits the generation of p-type carriers and also limits the hole mobility. The first p-type oxide of CuAlO₂ appeared in 1997 by Kawazoe and Hosono *et al.*²⁵. They considered hybridized orbitals between O 2*p* and Cu 3*d* in order to extend the VBM where energy states of Cu 3*d* orbitals locate near the O 2*p*, which offers a favorable environment to form hybrid orbitals²⁸. P-type oxide semiconductors such as CuAO₂ (A = B, Al, Ga, and In), SrCu₂O₂, and LaCuOX (X = S and Se) were produced^{25, 29-31} and similar electronic structures were also found in Cu₂O³² and Ag₂O³³. Efforts to implement these p-type oxides in devices such as p-channel thin film transistors were made; however, the required properties for device applications (e.g., mobility or carrier density) were difficult to tune and the devices were not functional^{26, 33-34}.

Ogo *et al.*²⁶ suggested that pseudo-closed ns^2 -orbitals near the VBM would produce oxides with p-type conduction. Such electronic structures are found in oxides incorporating heavy metal cations, such as Sn^{2+} ($5s^2$), Pb^{2+} ($6s^2$), and Bi^{3+} ($6s^2$), primarily because these elements are stable in ns^2 ($n \ge 5$) pseudo-closed shell electronic configurations. Among the suggested heavy metal cation oxides, PbO^{35} and Bi-related oxides³⁶ have been found to also not generate functioning devices, possibly due to an unfavorable electronic structure for PbO^{35} and deep level locations of Bi 6s orbitals in the valence band for Bi-O system³⁷. Instead, a simple binary oxide (SnO_x , x < 2) was found to be a good candidate for a p-type semiconductor due to its Sn 5s nature near the VBM and the possible formation of ns^2 hybrid orbitals, demonstrating high carrier mobilities (μ) of ~ 0.1 -2.5 cm²/Vs and carrier density ranging from $\sim 10^{17}$ to 10^{18} /cm³. 26 , $^{38-39}$ Martins *et al*. reported a first demonstration of oxide-based complementary metal-oxide-semiconductor

devices, consisting of p-SnOx (μ =0.8 cm²/Vs)and n-IGZO TFTs (μ =21 cm²/Vs) on papers for potential applications in disposable bio electronics.⁴⁰ More recently, Liu *et al.* demonstrated a low temperature (150-300 °C) processing of p-type Cu-doped NiO through solution combustion synthesis and its integration in TFTs, exhibiting μ =1.5 cm²/Vs and on/off current ratio of ~10⁴.⁴¹

As fundamental units in modern microelectronics, p-n junctions are widely used in electronic and optoelectronic applications such as junction transistors⁴², solar cells⁴³, photodetectors⁴⁴, electronic memory elements⁴⁵, and chemical sensors⁴⁶. Although single-crystalline bulk materials such as Si and GaAs have dominated the semiconductor junction industry and their applications, because of the demands of mild thermal budget processing, new or additional functionalities required for specific applications (e.g., transparency, catalytic activities), and low-cost manufacturing processes, oxide semiconductor thin films have been garnering a large amount of attention in recent years due to the results of enhanced understanding and processability of p-type oxides.

Although efforts have been made to realize oxide-based p-n heterojunctions, the majority of the previous studies exploited a thin film epitaxial growth technique (known as molecular beam epitaxy, MBE) or a high-powered laser beam process (known as pulsed laser deposition, PLD). While these methods have demonstrated the promising feasibility of oxide-based p-n junction applications, the general nature of these two techniques, such as the ultra-high vacuum requirements, high power usage and processing inability over large areas, limits further industrial and engineering applications of the demonstrated p-n heterojunctions. The particular benefits of these high-end techniques may include high quality thin films with minimal structural and electronic defects that lead to enhanced charge blocking performance for the reverse current and

consequently higher rectification behavior. Unlike TFTs, which is a single polarity device that consists of a high-performance dielectric layer to block the charge flow across the dielectric and hence modulate the conductance of the channel (mostly single polarity semiconducting active layer) by the gate field applied, the charge blocking performance in the p-n junction is the key parameter since the blocking performance is solely dependent on their own properties of produced p- and noxides without any additional or external assistance. Therefore, other conventional thin film processing methods such as sputtering, which are more compatible with industrial manufacturing processes, were initially limited to yield thin films with a non-negligible number of defects, and consequently resulted in poor rectifying behaviors. Oxide-based p-n heterojunctions exploiting MBE or PLD techniques demonstrated an on/off rectifying ratio ranging from 10-10² (still majority from such as p-SrCu₂O₂/n-ZnO, p-ZnRh₂O₄/n-ZnO, p-CuAlO₂/n-ZnO)⁴⁷⁻⁵¹ to 10³-10⁶ (such as p-ZnCo₂O₄/n-ZnSnO₂, p-NiO/n-In₂O₃:Mg₂, p-ZnCo₂O₄/n-In₂O₃:Mg₂)⁵²⁻⁵³, and some showed even higher than 108 from p-n junctions including p-ZnCo₂O₄/n-ZnO and p-NiO/n-ZnO.⁵⁴ In comparison, sputtering, evaporation or sol-gel processes predominantly yielded a rectifying performance less than ~10² out of p-NiO/n-ZnO⁵⁵, p-AgCoO₂/n-ZnO⁵⁶, p-SrCu₂O₂/n-ZnO⁵⁷, and p-SnO/n-ZnO⁵⁸. Although only a few sputter-only processed oxide p-n heterojunctions achieved an on/off ratio of 10³-10⁴, the further advancement of these oxide heterojunctions was limited due to either high reverse saturation current (or current density) or non-ideal performance, leading to difficulties using these favorable manufacturing techniques for the development of p-n heterojunctions.45

InGaZnO (IGZO) is a well-known n-type amorphous oxide semiconductor (AOS) that has been intensely investigated for oxide-based TFTs as a channel layer due to its high carrier mobility (5-

10 cm²/Vs), optical transparency in the visible regime (>~90%), and mild thermal budget processing (200-400 °C). Unlike covalent semiconductors such as amorphous Si, the demonstrated high carrier mobility of AOSs including IGZO is attributed to the localized conduction band minimum on spherically symmetrical metal s-states, and therefore, no significant impacts of the disordered nature are observed in the conduction behaviors. ⁵⁹⁻⁶⁰ This amorphous oxide semiconductor (AOS) is now being implemented in high performance activematrix liquid crystal displays, active-matrix organic light emitting diodes, and more recently in radio-frequency identification devices.⁶¹ Previous reports on forming Schottky metal contacts with IGZO to realize rectifying behaviors are also available in the literature.⁶² In AOS-based TFT fabrication, post-process annealing is often considered to improve charge carrier transport²⁰, contact properties at the semiconductor/metallization interface⁶, and TFT performance stability⁶³. Specifically, it has been reported that the stability of IGZO and other In₂O₃-based AOSs is significantly enhanced after approximately 400 °C annealing in air, which effectively reduces defects and trap density⁶³ of AOS materials. When considering p-n heterojunction application, the reduced defect/trap density and the enhanced stability may mitigate, at least in part, the issues of relatively poor charge blocking performance and hence rectifying behavior of sputterprocessed or solution-based oxide-based p-n diodes.

The present study aims to demonstrate high performance p-n heterojunctions based on room-temperature sputter-deposited p-SnOx and n-IGZO, of which the fabrication processes are compatible with other current standard manufacturing processes that require low thermal budget processing, moderate vacuum conditions, and scalability. The formation of *p*-SnO_x is systematically investigated through amorphous/crystalline diffraction analysis, optoelectronic

property evaluations, and work function and valence band measurements. The oxide p-n heterojunctions exhibit high rectification performance with an on/off ratio greater than 10^3 at ± 3 V, low reverse saturation current ($\sim 2 \times 10^{-10}$ A) and small turn-on voltage (~ 0.5 V). The achieved processing capability of p-SnO_x and the high diode performance may be significant to studies that seek a simple and reproducible strategy for p-type oxide processing and bipolar device applications with favorable processing techniques that are compatible with standard vacuum manufacturing methods.

2. Experimental details

Oxide thin films of p-SnO_x and n-IGZO were deposited using dc/rf magnetron sputtering on Si and glass substrates at room temperature. Substrates were first loaded to a load-lock chamber and after reaching a pressure of $<1\times10^{-3}$ Torr in the load-lock chamber, the substrates were transferred to the main chamber. During depositions, the substrates were rotated at 5 rpm to result in high uniformity and surface homogeneity. Prior to depositions, the sputter chamber was pumped down to a base pressure of $<3.5\times10^{-7}$ Torr and the target surface was pre-sputtered for 5-10 mins to remove target surface contamination and obtain uniform sputter gas flow. SnO_x thin films were deposited using reactive sputtering from a metal Sn target (99.999%, Kurt J. Lesker) at a dc power of 30W and at an Ar/O₂ sputter gas ratio of 88/12. During SnO_x depositions, the chamber working pressure was maintained at 2.0×10^{-3} Torr. IGZO thin films were sputtered using rf sputtering from a sintered IGZO target (In:Ga:Zn=1:1:1 in at%, 99.99%, Kurt J. Lesker) at an rf power of 70W and at a working pressure of 2.2×10^{-3} Torr at an Ar/O₂ ratio of 89/11.

Oxide-based hetero-junction p-n diodes were fabricated using the p-SnOx and n-IGZO films. Heavily-doped (100) p-Si⁺⁺ (0.003–0.005 Ω cm) was used as the p-side electrode as well as the substrate. SnOx was deposited on p-Si wafers as the p-type layer and annealed in air. Then, IGZO was deposited as the n-type material on p-SnOx/Si⁺⁺ wafers and annealed in air at 400 °C. Sn , as the n-side electrode, was deposited using dc sputtering at a dc power of 50W and at a chamber pressure of 2.7×10^{-3} Torr with pure Ar as the sputter gas. Each layer of p-SnOx, n-IGZO, and Sn was patterned through shadow masks. Heterojunction p-n diode characteristics were evaluated with a semiconductor parameter analyzer (Agilent 4155B) in a light-tight probe station under ambient air conditions. During the p-n junction measurements, the p-side electrode (heavily-doped p-Si) was grounded and the n-side electrode (Sn) was applied by bias ranging from -3 to 3 V. More than 15 devices were fabricated and tested to gather reliable data and provide evidence of reproducibility.

X-Ray diffraction (XRD) spectra to evaluate the amorphous and crystalline structures of the SnO_x and IGZO films were taken utilizing a Malvern Panalytical Empyrean X-Ray Diffractometer with a theta-two theta coupled scan mode. XRD investigations were made through Cu K α radiation (λ =1.54 Å) at a generator voltage of 45 kV and a tube current of 40 mA. Optoelectronic properties of the used oxide thin films, grown on glasses, were investigated in a UV-Vis spectrometer (Varian Cary 50) in the visible regime of 300-900 nm. A spotless bare glass piece was used for a baseline scan to exclude the substrate information in the resulting UV-Vis spectra. Film thickness was measured with a multiwavelength ellipsometer (FilmSense FS-1) using an incident and detection angle of 65°. Surface root-mean-square (RMS) roughness and topographic microstructures of SnO_x and IGZO films were analyzed via atomic force microscopy

(AFM) utilizing a Veeco Dimension 3100 microscope in tapping mode. Images were taken over 1 μm x 1 μm area using a Si cantilever (Bruker, tip frequency of 330 kHz). Scanning electron microscopy (SEM) was also utilized to examine microstructure evolution of SnOx and IGZO samples before and after annealing. Plan-view and cross-sectional SEM images were obtained utilizing a ThermoFisher Scientific Teneo SEM with a Trinity Detection System at magnifications between 100,000-160,000×. The electrical properties (e.g., carrier concentration and Hall mobility) of SnO_x and IGZO films were characterized from Hall Effect measurements in the van der Pauw configuration with a small specimen current (~1 nA) for which a magnetic-field variable electromagnet (0-2 Tesla, GMW Associates) and a bipolar power supply (KEPCO Inc.) were used.

X-ray photoelectron spectroscopy (XPS) investigations were made on p-SnO_x and n-IGZO films deposited on Si substrates to investigate the chemical environments and valence states of the major elements. XPS measurements were conducted in a Thermo Fisher Scientific NEXSA spectrometer under high vacuum ($<1 \times 10^{-7}$ Torr) with focused monochromatic soft Al $K\alpha$ x-ray radiation at 1486.6 eV. Prior to XPS measurements, the sample surface was cleaned for 15 secs by cluster Ar ions (Ar_n⁺) to remove any surface contaminants and to objectively evaluate the surface properties of the films without any interference. It should be noted that the cluster ion source (cluster energy of 4 eV/nucleon and cluster size of 1000) was employed to limit any chemical damages such as reduction of the oxide due to, known as, preferential sputtering. The work functions (Φ) of the oxide films were identified by ultraviolet photoelectron spectroscopy (UPS), integrated with the NEXSA spectrometer, using a monochromatic He (I) excitation at

21.22 eV. During UPS measurements, SnO_x and IGZO films were negatively biased with respect to earth ($V_{bias} = -7 \text{ V}$) by the conducting sample stage, through which the photoemitted electrons are accelerated and hence the onset of emission is detected. Before the measurements of SnO_x and IGZO samples, silver ($\Phi_{Ag} = \sim 4.5 \text{ eV}$) was used as reference to calibrate the spectrometer (see Fig. S1) and the binding energy scale, which allows accurate determinations of cut-off energy and Fermi level position.

3. Results and discussion

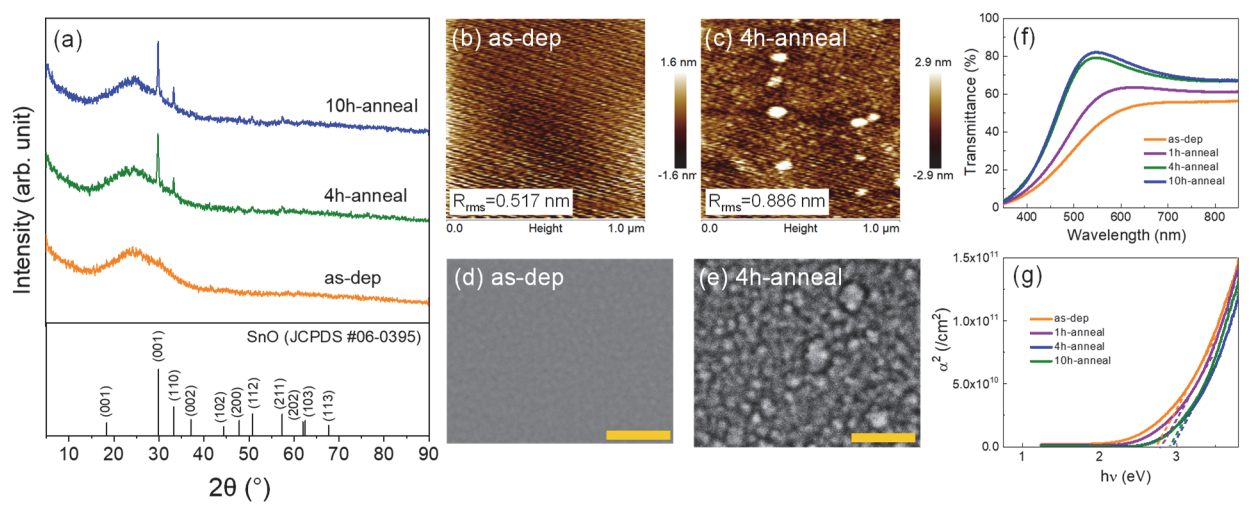


Figure 1. Thin film characteristics of SnO_x before and after annealing

(a) X-ray diffraction spectra obtained from as-deposited and annealed SnO_x films where the as-deposited curve indicates the amorphous phase of the film in its un-annealed state while the XRD spectra measured from annealed samples exhibit the poly-crystalline phase of SnO_x according to JCPDS #06-0395; AFM topographic images of SnO_x, measured from a scan area of $1 \times 1 \ \mu m^2$ of the image of (b) as-deposited SnO_x (R_{rms}=0.517 nm) with no significant micro features and (c) annealed at 300 °C in air exhibiting microstructure evolutions (R_{rms}=0.886 nm); SEM images of SnO_x thin films of (d) as-deposited and (e) annealed at 300 °C showing a similar microstructure evolution after annealing. The inset scale bars represent 500 nm; UV-Vis optoelectronic properties of (f) visible-regime transmittance of SnOx with annealing time and (g) optical bandgap extraction from Tauc plots for the direct transition, α^2 vs. hv.

Amorphous/crystalline structures of the SnO_x films were evaluated through XRD investigations and the results are shown in **Figure 1**a. In the as-deposited state (bottom), no significant

crystallographic features are observed, from which the as-deposited SnO_x is identified as the amorphous state. However, after annealing in air at 400 °C for 4 h, an amorphous-to-crystalline phase transformation is obviously observed in the diffraction spectra of annealed samples (middle and upper). A strong peak is seen at a diffraction angle of approximately 29.95°, which is attributed to the characteristic crystalline diffraction of the SnO (101) plane (JCPDS #06-0395). The XRD spectra obtained from annealed samples also show a peak at 2θ =33.37° diffracted from the SnO (110) plane. Other minor peaks are also detected at diffraction angles of 47.60°, 50.82°, and 57.57° which result from the SnO crystallographic planes of (200), (112), and (211), respectively. Quantitative analysis of the amorphous to crystalline diffraction peak intensity ratio shows no significant changes between 4 h- and 10 h-annealed samples, indicating that the majority of amorphous-to-crystallization reaction of SnO_x was completed within four hours of annealing. According to the XRD results, in order to ensure the completion of the crystallization, sputtered SnO_x films were annealed for at least 4 h for oxide-based p-n heterojunction applications demonstrated in the present study. The electrical properties of SnO_x were evaluated using small current Hall effect measurements. While Hall effect measurements on as-deposited SnO_x films were not consistent possibly due to the disordered nature and its associated tail states, reliable results were obtained from annealed SnO_x samples. The carrier density and mobility of annealed SnO_x were measured to be $3.1x10^{17}$ /cm³ and 1.91 cm²/Vs, respectively.

Surface topographic microstructures of SnO_x were investigated using AFM and the results were compared before and after annealing (4 h in air at 400 °C). The as-deposited AFM surface image in Figure 1b is smooth and devoid of microstructure features, which accounts for the amorphous

nature of the as-deposited SnO_x as identified by XRD (Fig. 1a). The as-deposited amorphous surface shows the root-mean-square roughness (R_{rms}) of 0.517 nm. However, the annealed AFM micrograph clearly displays surface microstructures that were evolved due to annealing. The microstructures shown in the annealed AFM image are the results from the amorphous-tocrystalline transformation and engendered poly-crystalline grains as identified in the annealed XRD spectra (Fig. 1a). In spite of the presence of crystalline features which emerged after annealing, the surface R_{rms} of annealed SnO_x is only 0.886 nm, of which the smooth surface makes it favorable to form heterojunction p-n diodes by limiting interfacial scattering at the junctions of p-SnO_x/n-IGZO and heavily-doped Si/p-SnO_x in our device structure (see the schematic in Figure 3a). Figures 1d-e display the SEM plan-view images of SnO_x to investigate the effect of annealing on the microstructures as well as to complement the AFM analysis. Notable grain boundaries are observed in the annealed SEM image, which coincides with the XRD and AFM results that represent crystalline structures and generated grains after annealing. In regard to crystallite size, the annealed grains are shown to be approximately ~15-30 nm in diameter when measured via plan-view SEM imaging, which is in good agreement with the AFM images (Fig. 1b-c).

Optoelectronic properties of p-SnO_x were determined through UV-Vis measurements, for which ~100 nm-thick SnO_x films, deposited on coverslip glass substrates, were used. A baseline scan was conducted on bare coverslip glass to exclude the substrate information in the resulting UV-Vis spectra. Figure 1f plots the visible regime transparency of the SnO_x films as a function of annealing time and wavelengths ranging from 300 nm to 900 nm. The transmittance increases with increased annealing time, and the absorption edge shifts to the left (i.e., blue shift) and gets

sharper, indicating the material is transformed to a more ordered state, which is supported by the XRD results (Fig. 1a) that present the amorphous-to-crystalline phase transformation of SnO_x. It is worth noting that the increase in transparency and the edge shift is not prominent after 4 h annealing, which indicates that the annealing effect becomes insignificant and the SnO_x films reach a pseudo-equilibrium state after approximately 4 h annealing, which is also in agreement with the XRD trend. To evaluate the optical bandgap (E_g) of SnO_x, Tauc plots were constructed as a function of annealing time. Figure 1g displays Tauc plots of $\alpha^2 vs$. hv for the direct bandgap transition of the SnO_x films⁶⁴⁻⁶⁶, where α is the absorption coefficient and hv is the photon energy with Planck constant h and the light frequency v. The E_g is determined by extrapolating the linear portion of Tauc plots to the zero absorption. The direct E_g of the SnO_x films is found to be approximately 2.7 eV in the as-deposited state and slightly increases with annealing time, saturated to \sim 2.9 eV for the 10 h-annealed SnO_x. These direct E_g values of p-SnO_x are well matched with those (2.60-3.15 eV) found in the literature⁶⁴⁻⁶⁶. The polarity of the SnO_x films is found to be p-type for both as-deposited and annealed states through photoelectron spectroscopy, which is further detailed later in Figure 4a. The origin of the increase in the $E_{\rm g}$ after annealing is possibly due to the increase in carrier density after annealing, which is experimentally supported by the valence band measurements, of which the detailed discussion is provided later in Figure 4b.

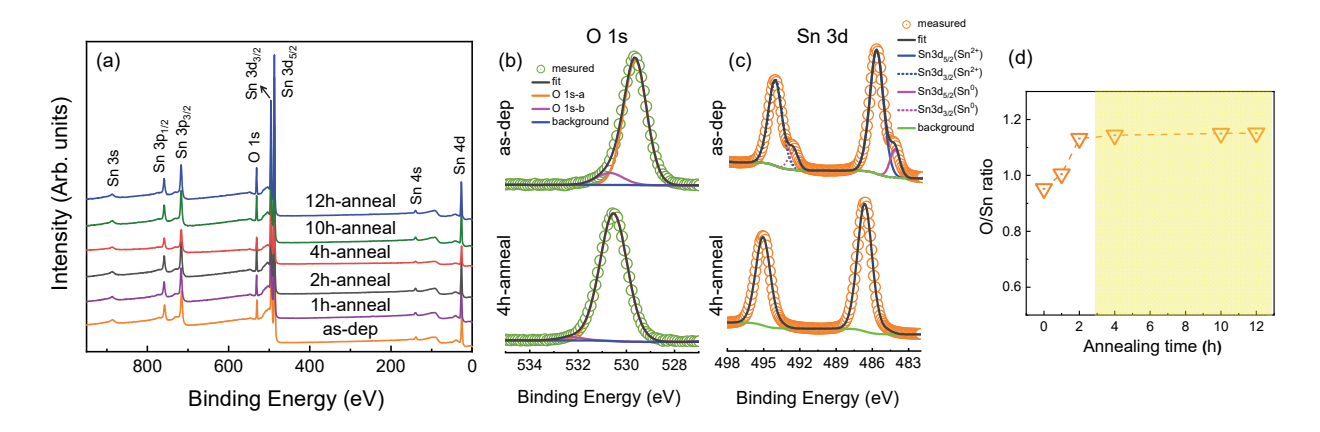


Figure 2. XPS chemical environment and valence state analysis of p-SnO_x (a) XPS survey scans of p-SnO_x films before and after annealing in air at 400 °C, where the survey spectra display peaks of O 1s and Sn 3d with other minor Sn-related peaks; core-level HR XPS spectra of (b) O 1s and (c) Sn 3d before (upper) and after (lower) annealing; and (d) the ratio of O/Sn as a function of annealing time, where the ratio is saturated after approximately 2 h of annealing.

XPS investigations were conducted and the results are shown in **Figure 2** to compare the elemental compositions and valence state of major elements in as-deposited and annealed SnO_x films. Figure 2a shows XPS survey scans of SnO_x thin films measured at binding energies ranging from 0 to 900 eV. All the survey spectra are similar to each other, where strong XPS detection from Sn 3d and O 1s is observed with other Sn-related peaks from Sn 3s, 3p, 4s and 4d excitations.

To further investigate the effect of annealing of SnO_x on the valence state of major elements of SnO_x films (i.e., O 1s and Sn 3d), core-level high resolution (HR) XPS analysis was performed as a function of annealing time. Core level HR O 1s XPS spectra are shown in Figure 2b. In the as-deposited state (upper), the HR O 1s spectrum exhibits slight asymmetry in the peak that is deconvoluted into two peaks, one at 529.64 eV (strong) due to lattice oxygens in SnO_x and another at 530.67 eV (weak) attributed to the presence of oxygen-related defects or hydroxyl group⁶⁷. After annealing (lower), the overall peak location shifted toward higher binding energy by approximately 0.94 eV, which results from the crystallization reaction during annealing,

leading to a higher binding energy of oxygen in the annealed SnO_x. It should also be noted that no significant asymmetry is observed in the annealed HR O 1s spectrum, which can be understood by the fact that the oxygen defects present in the as-deposited state were oxidized during annealing in air. Among the annealed samples (after 4 h) shown in Figure S5a, neither peak shifts nor asymmetry are identified in HR O 1s XPS plots measured from those with longer annealing time, indicating that the oxygen in SnO_x does not oxidize further.

Figure 2c shows HR XPS spectra of core-level Sn 3d to compare its valence state before and after annealing. The as-deposited XPS result (upper) exhibits two main peaks of Sn 3d_{5/2} at 485.79 eV and its spin-orbit split pair of Sn 3d_{3/2} at 494.22 eV, which results from the Sn²⁺ state in SnO. It should be noted that another peak is clearly visible as a shoulder on the right of both Sn 3d_{5/2} and 3d_{3/2} components, which is attributed to the Sn⁰ state from neutral (or metallic) Sn in the as-deposited SnO_x. The annelaed HR Sn 3d plot (lower) is symetric and no neutral Sn-related peaks/shoulders are detected in the annealed Sn 3d XPS results, which indicates that the annealed SnO_x films are devoid of metallic Sn phases (i.e., Sn⁰ state) due to the oxidation of neutral Sn during the annealing in air. As similarly shown in the HR O 1s XPS investigations, after annealing for 4 h, no further changes in the HR Sn 3d XPS plots were observed in Figure S5b, which is in good agreement with XRD and UV-Vis analyses, indicating that the oxidation reaction as well as the amorphous-to-crystallization process was completed after ~4 h annealing and the SnO_x samples reached the (pseudo-) equilibrium state.

The elemental composition ratio of O/Sn was determined through peak area analysis on the HR XPS spectra in Figure 2 b-c and the results are summarized in Figure 2d. The as-deposited ratio

is determined to be 0.951 and increased to 1.134 after 2 h anealing, and further increased up to 1.151 after 4 h annealing, of which the ratio remains nearly the same for the longer time annealed samples. The increase in the O/Sn ratio during air-annealing is obviously attributed to the oxidation of Sn that is present in the as-deposited state. This Sn oxidation is evidenced by the comparison between the HR Sn 3d XPS spectra before and after annealing. It should be noted that the O/Sn ratio is saturated to 1.151 after 4 h annealing and therefore the stoichiometry of our SnO_x is reasonably assumed to be SnO_{1.15}. This consistent O/Sn ratio after 4 h annealing well concurs with the (pseudo-) equilibrium state of the annealed SnO_x, which is also supported by the previous XRD, UV-Vis, and HR XPS (O 1s and Sn 3d) analyses, exhibiting no prominent changes in crystalline structure, optoelectronic properties and chemical environements.

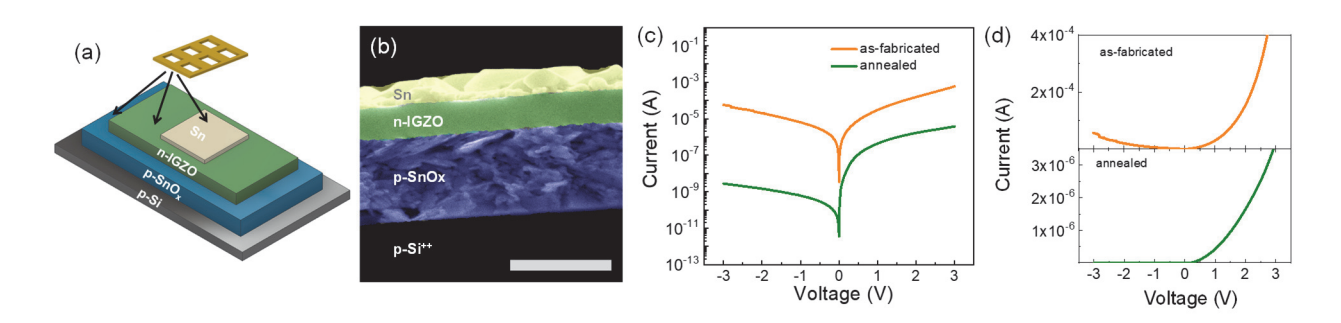


Figure 3. Oxide-based p-n heterojunction diodes and performance (a) Schematic illustration of device structure, consisting of heavily-doped p-Si as the substrate and bottom contact, p-SnO_x, n-IGZO and Sn top contact. The p-n heterojunction devices were fabricated through shadow masks to define each layer. (b) False color cross-sectional SEM micrograph of the oxide heterojunction that present clear layers of p-SnO_x and n-IGZO. The inset scale bars represent 500 nm. (c) log(I)-V characteristics of the heterojunction diode before and after annealing. And (d) linear scale I-V plots where the on-voltage of the heterojunction diode is determined to be ~0.5 V, which is close to the built-in potential of the p-n junction that is determined from work function measurements.

A schematic of the oxide-based heterojunction p-n diodes that integrate p-SnO_x (x=1.151 identified by XPS in this study) and n-IGZO (In:Ga:Zn=1:1:1 in at%) layers is illustrated in

Figure 3a and a false color cross-sectional SEM micrograph of the device is presented in Figure 3b where the thickness of p-SnO_x (~600 nm) and n-IGZO (~250 nm) used in this study was optimized by evaluating the diode performance of p-Si/n-IGZO and n-Si/p-SnO_x junctions as a function of SnO_x and IGZO thickness. The cross-sectional SEM image clearly shows the layered structure of oxide p-n junction on heavily-doped p-Si, in which the p-SnO_x cross-sectional view exhibits grain microstructures due to the polycrystalline nature as evidenced in the XRD spectra (Fig. 1) while the IGZO layer presents no micro features owing to its amorphous state (see Fig. S2).

The current-voltage characteristics of the p-SnOx/n-IGZO heterojunction devices was evaluated under dark by recording the current in response to voltage applied. The measured current (I) presented in Figure 3c relates the reverse saturation current (I_0), the ideality factor (n), the series resistance (R_s), and the shunt resistance (R_s) with the elementary charge (q) in the Shockley equation:

$$I = I_o \left\{ \exp \left[\frac{q}{nkT} (V - IR_s) \right] - 1 \right\} + \frac{V - IR_s}{R_{ch}}$$
 (1)

The oxide p-n heterojunction performance was evaluated and compared before and after annealing. Device performance measurements were made on more than 15 p-n junction devices, which demonstrate consistent I-V characteristics with minimal deviations. The typical results are shown in Figure 3c. Notice should be taken on the effect of annealing on the diode performance of the oxide-based heterojunction. The main differences in the diode parameters before and after annealing are two-fold: (i) the on/off rectification ratio was enhanced from $\sim 10^1$ (as-fabricated) to greater than 10^3 (4 h-annealed); and (ii) the reverse current decreased significantly from the as-deposited $\sim 5 \times 10^{-5}$ A at -3 V to $\sim 1 \times 10^{-9}$ A after annealing for 4 h, which is defined as the

off-state current. The pre-exponential factor I_0 critically depends on the impurity density that governs the carrier life time and plays a role as the base current of the forward diode current. The reduction in reverse-current, hence the on-current, of the heterojunction may be mainly attributed to the oxidation of the IGZO layer during air-annealing. We reported on the effect of air annealing on the doping concentration of amorphous oxides based on In₂O₃ such as InZnO and IGZO. Two competing mechanisms are responsible for the overall variations in carrier density and, hence, conductivity of these materials^{20, 68}: (i) amorphous relaxation and (ii) nativedefect based doping/de-doping. In our previous in-situ four-contact conductivity and kinetics analyses on these amorphous oxides during air-annealing, the oxidation of vacancies during annealing, which decreases the carrier density, is faster than the rate of local amorphous structural relaxation, although the overall rate of conductivity change is dependent on the diffusion distance (i.e., film thickness) and diffusivity²⁰. Since the annihilation of oxygen vacancy defects consumes two free carriers/vacancy, the oxygen vacancy mechanism supports the reduction in the on and off currents of the heterojunction diode shown in Figure 3c. The oxidation of vacancies and reduction in carrier density is in agreement with Hall effect measurements, showing about an order of magnitude decrease in carrier density of IGZO after annealing (as-deposited 4.71×10^{17} /cm³ vs annealed 5.96×10^{16} /cm³). The carrier density decrease in IGZO is further supported by the valence band investigations in Figure 4, which identify the location of valence band maximum with respect to the Fermi level position. The valence band investigations of SnO_x and IGZO will be further discussed later in the heterojunction band alignment section.

The ideality factor of the oxide-based heterojunctions was extracted by fitting equation 1 in the forward-bias direction and was found to be 2.87 for the as-deposited and 2.53 for the annealed heterojunction diodes. Since a lower ideality factor is achieved from materials with low defect density, the obtained lower ideality factor after annealing also partly supports the discussion above, describing a decrease in carrier density in n-IGZO. Other device parameters fitted by Eq. (1) are summarized in **Table 1**. The series resistance increases about five times after annealing, which points toward the evidence of lower carrier density in annealed IGZO. The shunt resistance was enhanced more than ~70 times after annealing, mainly due to the reduction of the current paths across the junction, which also partly supports the notion of the decrease in the defect density after annealing. In addition, the performance of the oxide-based p-n junctions after annealing remains nearly the same over time in air. The stability is attributed to the employment of SnO_x with a completed phase transformation reaction (as evidenced by XRD and XPS in Fig. 1 and 2) as well as the reduced trap density in IGZO. A change in the trap density of IGZO is detailed by work function and valence band investigations later with Figure 5.

Table 1. Summary of diode parameters extracted from I-V characteristics

	Ideality factor	Saturation Current	Series Resistance	Shunt Resistance
	(n)	$I_{\theta}\left(\mathbf{A}\right)$	$R_{s}\left(\Omega ight)$	$R_{sh}\left(\Omega\right)$
as-dep	2.87 ± 0.18	2.99±0.46 ×10 ⁻⁹	$7.65\pm1.12\times10^{2}$	$1.41\pm0.66 \times 10^5$
anneal	2.53 ± 0.11	2.09±0.31 ×10 ⁻¹⁰	$3.04\pm0.84 \times 10^{3}$	$8.18\pm0.19 \times 10^6$

The turn on voltage can be estimated by a linear fit of the linear scale forward bias I-V performance shown in Figure 3d. Both of the as-deposited and annealed devices are turned on at a relatively low bias of approximately 0.5 V, which is close to the built-in potential of the oxide-based heterojunction. The low turn-on voltage implies a low voltage drop at the p-n junction,

which leads to low power consumption in practical applications. Sharper turn-on behaviors of the p-n heterojunction were observed after annealing, which is attributed to the reduced defect state density after annealing. The origin of the turn-on voltage is further discussed with the built-in potential determined by the band structure and energy level investigations of p-SnO_x and n-IGZO studied through photoelectron spectroscopy.

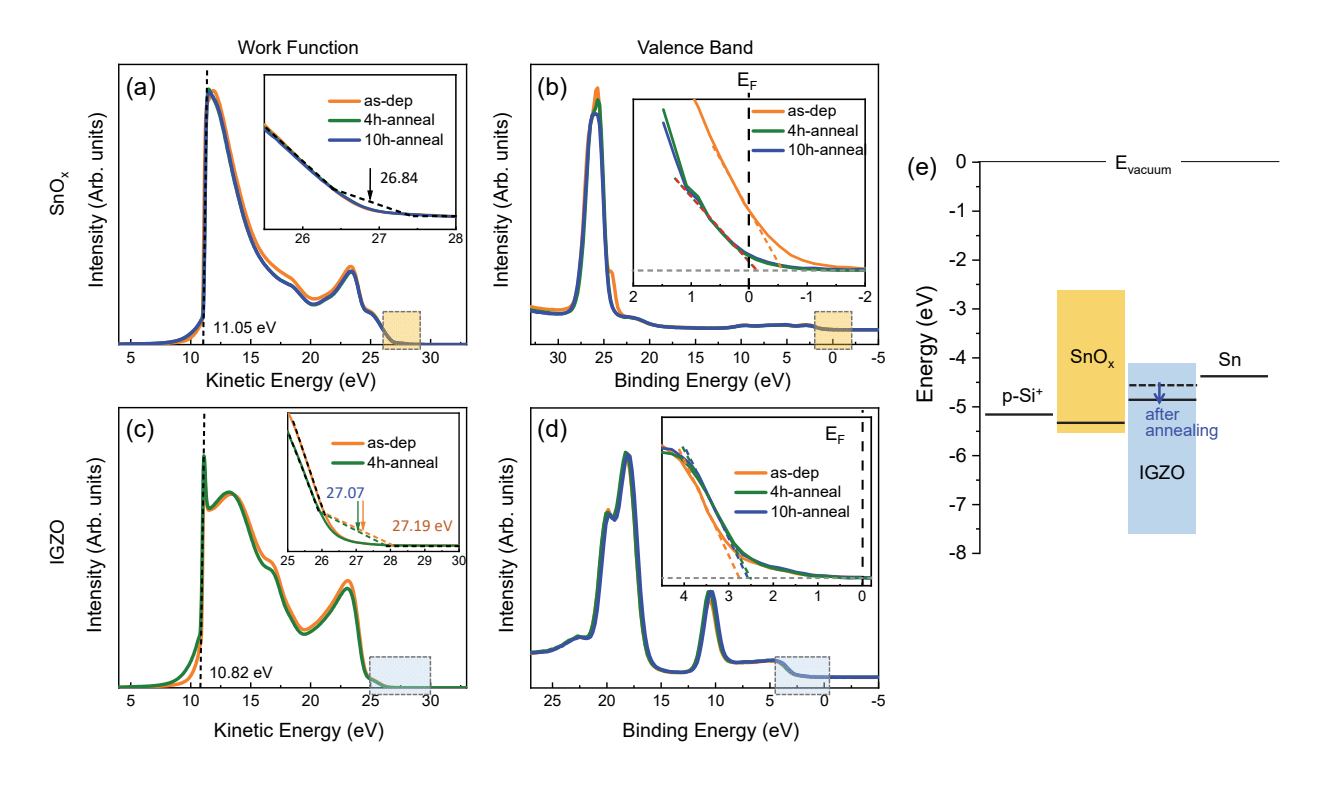


Figure 4. Work function and valence band measurements through photoelectron spectroscopy (a) UPS investigations of SnO_x before and after annealing from which the $Φ_{SnOx}$ is identified as 5.42 eV with $E_{cut-off}$ and $E_{F,edge}$ of 11.05 and 26.84 eV, respectively. (b) VBM measurements of SnO_x before and after annealing where the (E_F-E_V) of the SnO_x decreases from 0.58 eV to 0.13 eV after annealing, indicating higher doping in p-type SnO_x after annealing. (c) UPS spectra measured from IGZO films before and after annealing where the $Φ_{IGZO}$ is found to be 4.76 eV for the as-deposited and 4.97 eV for the annealed. (d) VBM investigations of IGZO where the (E_V-E_F) decreases from 2.81 eV to 2.54 eV, representing dedoping in n-type IGZO after annealing. (e) Energy level alignment of the oxide-based p-n heterojunction according to the work function and VBM results. Note that the work function difference (ΔΦ) between SnO_x and IGZO, which is the built-in potential in p-n junctions is reduced after annealing.

An energy band structure was constructed to further understand the diode behaviors of the oxide heterojunction and the polarity of the p- and n-type oxides through measurements of work function, valence band maximum, and bandgap of each material. The work function (Φ) is identified using UPS with the photon energy (hv=21.22 eV from He I source), the cut-off kinetic energy ($E_{cut-off}$) that is the energy of free electrons generated by the photoelectric effect, and the Fermi edge position ($E_{F,edge}$) via the equation:

$$\Phi = hv + E_{cut-off} - E_{F,edge} \tag{2}$$

The UPS results of SnO_x before and after annealing are shown in **Figure 4**a from which the cutoff kinetic energy of as-deposited SnO_x is found to be approximately 11.05 ± 0.05 eV. An
extended spectrum (KE from 25 to 28 eV) is also presented as inset of Figure 4a where the Fermi
edge location of as-deposited SnO_x is estimated to be ~26.84 \pm 0.11 eV. According to the
determined $E_{cut\text{-}off}$ and E_F position, the Φ of the as-deposited SnO_x film in this study is calculated
as 5.421 ± 0.02 eV. Similarly, the work function of annealed SnO_x was also determined to be 5.428 eV, which is nearly the same as that of the as-deposited SnO_x (only 0.12% change after
annealing).

Figure 4b exhibits the valence band maximum (VBM) location of SnO_x determined by XPS, representing the effect of annealing on the VBM of SnO_x. The peaks located around 26 eV are indicative of the Sn 4d band, as similarly shown in the XPS survey scans. The as-deposited VBM spectrum shows a shoulder originated from Sn⁰ on the right of the main peak, which concurs with the HR Sn 4d XPS of the as-deposited SnO_x (Figure 2c). An inset shows an extended view of the plots where the straight-line intersection points with the baseline indicate the onset of photoexcitation, which gives the VBM energy level, E_V, in

relation to the Fermi energy level, E_F (E_F is simply located at 0 eV since the E_F of the sample and spectrometer are equalized.)⁶⁹⁻⁷⁰. The VBM of the as-deposited SnO_x is estimated to be ~0.57±0.01 eV lower than that of the Fermi level (i.e., E_F-E_V=0.57 eV), clearly evidencing the p-type conduction behavior despite the amorphous state of the as-deposited SnO_x. After annealing, a noteworthy shift of the VBM of SnO_x is observed towards the E_F in the plot, which indicates that the doping in p-SnO_x increases after annealing. After 4 h annealing, the VBM shift becomes insignificant and the VBM spectra of the 4 h and 10 h annealed samples are nearly overlapped with each other, further relating that the p-SnO_x reached the pseudo saturation state in doping after 4 h annealing, which is supported by other evaluations in this study through XRD (Fig. 1a), UV-Vis (Fig. 1f,g) and XPS (Fig. 2). It should be noted that the all oxide p-n junctions in this study were fabricated from SnO_x annealed for at least 4 h to obtain stable device performance and also to objectively extract performance parameters without any variations of SnO_x properties.

The work function and VBM of n-IGZO were similarly determined as those described above for p-SnO_x. The IGZO work function in Figure 4c was changed from as-deposited 4.85±0.02 eV to 4.97±0.02 eV after annealing, while the VBM of IGZO displayed in Figure 4d decreases from 2.76±0.03 eV to 2.55±0.02 eV. According to the Φ and VBM measured from IGZO before and after annealing, it is clearly identified that the E_F of IGZO after annealing moved toward the VBM, indicating that the carrier density of IGZO decreased after annealing. The confirmed lower doping level in IGZO after annealing aligns well with the I-V characteristics in Figure 3c, showing decreases in both on- and off-current.

With the values of Φ , VBM and E_g of p-SnO_x and n-IGZO, the energy band structure representing energy levels within the oxide heterojunctions was constructed and is shown in Figure 4e. The constructed energy diagrams confirm ohmic properties for the n-side while the pside is found to have pseudo-ohmic contact properties. The work function of heavily-doped p-Si (p-Si⁺⁺) is \sim 5.2 eV (with Si electron affinity, χ =4.05 eV and bandgap, E_g=1.12 eV) and the work function of SnO_x is determined to be ~5.4 eV in our study, which does not form an ideal ohmic contact. If a significant Schottky barrier is formed from the SnO_x/p-Si⁺⁺ contact, this will create a diode of opposite polarity with respect to the main p-n junction (SnO_x/IGZO junction). From an electrical point of view, this will create a back-to-back diode where the I-V characteristics will show non-rectifying, small currents on both forward and reverse bias regions because one of the diodes is always off whether in forward or reverse bias. However, strong rectifying behaviors evidenced in Figure 3d suggest a dominant electrical junction is formed by the main p-SnO_x/n-IGZO interface. The built-in potential of the oxide-based p-n heterojunction is identified to be approximately 0.57 and 0.46 eV for the as-deposited and annealed samples, respectively, which is estimated from the work function difference ($\Delta \Phi = \Phi_{IGZO} - \Phi_{SnOx}$). The determined built-in potential values are similar to the turn-on voltage (~0.5 V) of the p-n heterojunction, as discussed in Figure 3d, which is the potential barrier that the charge carriers have to overcome at the heterojunction.

4. Conclusions

We have demonstrated oxide-based heterojunction p-n diodes that consists of sputter-processed p-SnO_x and n-IGZO. The formation of poly-crystalline p-SnO_x films that are devoid of metallic Sn phases were confirmed by XRD, XPS and UPS and the resulting p-SnO_x was integrated in the

oxide-based p-n junction. To ensure the effective charge blocking performance in the p-n

heterojunctions, IGZO was selected as the n-type oxide for the p-n heterojunctions due to the

established knowledge that the defect/trap density is critically reduced after mild temperature

annealing at 400 °C. The oxide-based p-n heterojunction exhibits a high on/off ratio, greater than

 10^3 , small saturation current as low as $\sim 2 \times 10^{-10}$ A, and an ideality factor of 2.53 after annealing

with excellent stability over time in air. Particularly, the demonstrated high performance oxide-

based p-n diodes can be processed via sputtering technique, which is compatible with standard

vacuum manufacturing methods that require mild thermal budget manufacturing. Therefore, the

outcomes of the current study are expected to contribute to the development of p-type oxides

and their industrial device applications such as p-n diodes of which the manufacturing routes are

in-line with the current processing requirements.

ASSOCIATED CONTENT

Supporting Information. UPS work function measurements from Ag as reference for the

calibration of the spectrometer and the binding energy scale; XRD spectra obtained from as-

deposited and annealed (400 °C in air for four hours) IGZO films; AFM and SEM images of as-

deposited d and annealed IGZO; Core-level HR XPS spectra of O 1s and Sn 3d obtained from

SnO_x films as a function of annealing time; UV-Vis measurements of IGZO before and after

annealing. "This material is available free of charge via the Internet at http://pubs.acs.org."

AUTHOR INFORMATION

Corresponding Author

*Sunghwan Lee. Email: sunghlee@purdue.edu

Author Contributions

25

DH Lee and S Lee designed the experiments and wrote the manuscript; HH Park and HS Park conducted XPS and UPS measurements; M Clevenger performed XRD and AFM measurements and analyses; H Kim and DK Ko contributed to the device performance measurements and analyses; CS Kim obtained electron microscope images; M Liu, G Kim and S Kim contributed to thin film depositions and processing optimizations; HW Song, K No and A Lucietto contributed to data analyses and writing the manuscript.

Notes

The authors declare no competing financial interest.

ACKNOWLEDGMENT

This work was supported by the U.S. National Science Foundation (NSF) Award No. ECCS-1931088. S.L. and H.W.S. acknowledge the support from the Improvement of Measurement Standards and Technology for Mechanical Metrology (Grant No. 20011028) by KRISS. K.N. was supported by Basic Science Research Program (NRF-2021R11A1A01051246) through the NRF Korea funded by the Ministry of Education.

References

- 1. Nomura, K.; Ohta, H.; Takagi, A.; Kamiya, T.; Hirano, M.; Hosono, H., Room-temperature Fabrication of Transparent Flexible Thin-film Transistors using Amorphous Oxide Semiconductors. *Nature* **2004**, *432* (7016), 488-492.
- 2. Ginley, D. S.; Hosono, H.; Paine, D. C., *Handbook of Transparent Conductors*. Springer US: New York, 2010; p 1-533.
- 3. Wager, J. F., Transparent Electronics. *Science* **2003**, *300* (5623), 1245-1246.
- 4. Paine, D. C.; Whitson, T.; Janiac, D.; Beresford, R.; Yang, C. O.; Lewis, B., A Study of Low Temperature Crystallization of Amorphous Thin Tilm Indium-Tin-Oxide. *Journal of Applied Physics* **1999**, *85* (12), 8445-8450.
- 5. Dehuff, N. L.; Kettenring, E. S.; Hong, D.; Chiang, H. Q.; Wager, J. F.; Hoffman, R. L.; Park, C. H.; Keszler, D. A., Transparent Thin-film Transistors with Zinc Indium Oxide Channel Layer. *Journal of Applied Physics* **2005**, *97* (6).
- 6. Lee, S.; Park, H.; Paine, D. C., A study of the Specific Contact Resistance and Channel Resistivity of Amorphous IZO Thin Film Transistors with IZO Source-Drain Metallization. *Journal of Applied Physics* **2011**, *109* (6), 063702.
- 7. Ow-Yang, C. W.; Yeom, H.-y.; Paine, D. C., Fabrication of Transparent Conducting Amorphous Zn-Sn-In-O Thin Films by Direct Current Magnetron Sputtering. *Thin Solid Films* **2008**, *516* (10), 3105-3111.
- 8. Lee, C.-G.; Cobb, B.; Dodabalapur, A., Band Transport and Mobility Edge in Amorphous Solution-processed Zinc Tin Oxide Thin-film Transistors. *Appl. Phys. Lett.* **2010,** *97* (20), 203505.
- 9. Kikuchi, Y.; Nomura, K.; Yanagi, H.; Kamiya, T.; Hirano, M.; Hosono, H., Device Characteristics Improvement of a-In-Ga-Zn-O TFTs by Low-temperature Annealing. *Thin Solid Films* **2010**, *518* (11), 3017-3021.
- 10. Kamiya, T.; Hiramatsu, H.; Nomura, K.; Hosono, H., Device Applications of Transparent Oxide Semiconductors: Excitonic Blue LED and Transparent Flexible TFT. *Journal of Electroceramics* **2006**, *17* (2-4), 267-275.
- 11. Lee, S.; Kim, S.-H.; Kim, Y.; Kingon, A. I.; Paine, D. C.; No, K., Structural and Electrical Properties of Transparent Conducting Al2O3-doped ZnO Thin Films using Off-axis DC Magnetron Sputtering. *Materials Letters* **2012**, *85*, 88-90.
- 12. Jia, J.; Takasaki, A.; Oka, N.; Shigesato, Y., Experimental Observation on the Fermi Level Shift in Polycrystalline Al-doped ZnO Films. *J. Appl. Phys.* **2012**, *112* (1).
- 13. Oka, N.; Kimura, K.; Yagi, T.; Taketoshi, N.; Baba, T.; Shigesato, Y., Thermophysical and Electrical Properties of Al-doped ZnO Films. *J. Appl. Phys.* **2012**, *111* (9).
- 14. Hsieh, H.-H.; Wu, C.-C., Scaling Behavior of ZnO Transparent Thin-film Transistors. *Appl. Phys. Lett.* **2006**, *89* (4), 041109.

- 15. Yaglioglu, B.; Yeom, H. Y.; Beresford, R.; Paine, D. C., High-mobility Amorphous In2O3-10 wt %ZnO Thin Film Transistors. *Applied Physics Letters* **2006**, *89* (6), 062103.
- 16. Lee, S.; Paine, D. C., Metallization Selection and the Performance of Amorphous In-Zn-O Thin Film Transistors. *Applied Physics Letters* **2014**, *104* (25), 252103.
- 17. Barquinha, P.; Martins, R.; Pereira, L.; Fortunato, E., *Transparent Oxide Electronics: From Materials to Devices*. Wiley: 2012.
- 18. Olziersky, A.; Barquinha, P.; Vilà, A.; Magaña, C.; Fortunato, E.; Morante, J. R.; Martins, R., Role of Ga2O3–In2O3–ZnO Channel Composition on the Electrical Performance of Thin-film Transistors. *Materials Chemistry and Physics* **2011**, *131* (1), 512-518.
- 19. Paine, D. C.; Yaglioglu, B.; Beiley, Z.; Lee, S., Amorphous IZO-based Transparent Thin Film Transistors. *Thin Solid Films* **2008**, *516* (17), 5894-5898.
- 20. Lee, S.; Bierig, B.; Paine, D. C., Amorphous Structure and Electrical Performance of Low-Temperature Annealed Amorphous Indium Zinc Oxide Transparent Thin Film Transistors. *Thin Solid Films* **2012**, *520* (10), 3764-3768.
- 21. Lee, S.; Park, K.; Paine, D. C., Metallization Strategies for In2O3-based Amorphous Oxide Semiconductor Materials. *Journal of Materials Research* **2012**, *27* (17), 2299-2308.
- 22. Kamiya, T.; Nomura, K.; Hosono, H., Origins of High Mobility and Low Operation Voltage of Amorphous Oxide TFTs: Electronic Structure, Electron Transport, Defects and Doping. *Journal of Display Technology* **2009**, *5* (12), 468-83.
- 23. Lee, H. N.; Kyung, J. W.; Kang, S. K.; Kim, D. Y.; Sung, M. C.; Kim, S. J.; Kim, C. N.; Kim, H. G.; Kim, S. T.; Ite, *Current Status of, Challenges to, and Perspective View of AM-OLED*. 2006; p 663-666.
- 24. Fortunato, E.; Ginley, D.; Hosono, H.; Paine, D. C., Transparent Conducting Oxides for Photovoltaics. *MRS Bull.* **2007**, *32* (3), 242-247.
- 25. Kawazoe, H.; Yasukawa, M.; Hyodo, H.; Kurita, M.; Yanagi, H.; Hosono, H., P-type Electrical Conduction in Transparent Thin Films of CuAlO2. *Nature* **1997**, *389* (6654), 939-942.
- 26. Ogo, Y.; Hiramatsu, H.; Nomura, K.; Yanagi, H.; Kamiya, T.; Hirano, M.; Hosono, H., P-channel Thin-film Transistor using P-type Oxide Semiconductor, SnO. *Applied Physics Letters* **2008**, *93* (3), 032113.
- 27. Meng, J.; Jena, P.; Vail, J. M., Hole Trapping in LIXNI1-XO. *Journal of Physics-Condensed Matter* **1990**, *2* (51), 10371-10377.
- 28. Kawazoe, H.; Yanagi, H.; Ueda, K.; Hosono, H., Transparent p-Type Conducting Oxides: Design and Fabrication of p-n Heterojunctions. *MRS Bull.* **2000,** *25* (08), 28-36.
- 29. Kawazoe, H.; Yanagi, H.; Ueda, K.; Hosono, H., Transparent P-type Conducting Oxides: Design and Fabrication of p-n Heterojunctions. *MRS Bull.* **2000**, *25* (8), 28-36.
- 30. Snure, M.; Tiwari, A., CuBO2: A P-type Transparent Oxide. *Appl. Phys. Lett.* **2007**, *91* (9).
- 31. Ueda, K.; Hosono, H., Band Gap Engineering, Band Edge Emission, and P-type Conductivity in Wide-gap LaCuOS1-xSex Oxychalcogenides. *J. Appl. Phys.* **2002**, *91* (7), 4768-4770.

- 32. Ogo, Y.; Hiramatsu, H.; Nomura, K.; Yanagi, H.; Kamiya, T.; Kimura, M.; Hirano, M.; Hosono, H., Tin Monoxide as an s-orbital-based P-type Oxide Semiconductor: Electronic Structures and TFT application. *Physica Status Solidi a-Applications and Materials Science* **2009**, *206* (9), 2187-2191.
- 33. Barik, U. K.; Srinivasan, S.; Nagendra, C. L.; Subrahmanyam, A., Electrical and Optical Properties of Reactive DC magnetron Sputtered Silver Oxide Thin Films: Role of Oxygen. *Thin Solid Films* **2003**, *429* (1-2), 129-134.
- 34. Hiramatsu, H.; Ueda, K.; Ohta, H.; Hirano, M.; Kamiya, T.; Hosono, H., Degenerate Ptype Conductivity in Wide-gap LaCuOS1-xSex (x=0-1) Epitaxial Films. *Appl. Phys. Lett.* **2003**, 82 (7), 1048-1050.
- 35. Mizoguchi, H.; Kawazoe, H.; Hosono, H., Enhancement of Electrical Conductivity of Polycrystalline β-PbO by Exposure to Ozone Gas at Room Temperature. *Chem. Mater.* **1996**, *8* (12), 2769-2773.
- 36. Madelung, O., Semiconductors: Data Handbook. Springer Berlin Heidelberg: 2004.
- 37. Hiramatsu, H.; Yanagi, H.; Kamiya, T.; Ueda, K.; Hirano, M.; Hosono, H., Crystal Structures, Optoelectronic Properties, and Electronic Structures of Layered Oxychalcogenides MCuOCh (M = Bi, La; Ch = S, Se, Te): Effects of Electronic Configurations of M3+ Ions. *Chem. Mater.* **2008**, *20* (1), 326-334.
- 38. Yabuta, H.; Kaji, N.; Hayashi, R.; Kumomi, H.; Nomura, K.; Kamiya, T.; Hirano, M.; Hosono, H., Sputtering Formation of P-type SnO Thin-film Transistors on Glass toward Oxide Complimentary Circuits. *Applied Physics Letters* **2010**, *97* (7), 072111.
- 39. Hsu, P.-C.; Chen, W.-C.; Tsai, Y.-T.; Kung, Y.-C.; Chang, C.-H.; Hsu, C.-J.; Wu, C.-C.; Hsieh, H.-H., Fabrication of P-Type SnO Thin-Film Transistors by Sputtering with Practical Metal Electrodes. *Japanese Journal of Applied Physics* **2013**, *52* (5S1), 05DC07.
- 40. Martins, R.; Nathan, A.; Barros, R.; Pereira, L.; Barquinha, P.; Correia, N.; Costa, R.; Ahnood, A.; Ferreira, I.; Fortunato, E., Complementary Metal Oxide Semiconductor Technology With and On Paper. *Adv. Mater.* **2011**, *23* (39), 4491-4496.
- 41. Liu, A.; Zhu, H.; Guo, Z.; Meng, Y.; Liu, G.; Fortunato, E.; Martins, R.; Shan, F., Solution Combustion Synthesis: Low-Temperature Processing for p-Type Cu:NiO Thin Films for Transparent Electronics. *Adv. Mater.* **2017**, *29* (34), 1701599.
- 42. Streetman, B. G.; Banerjee, S. K., *Solid State Electronic Devices*. 6 ed.; Pearson Prentice Hall: 2006.
- 43. Iqbal, K.; Ikram, M.; Afzal, M.; Ali, S., Efficient, Low-dimensional Nanocomposite Bilayer CuO/ZnO Solar Cell at Various Annealing Temperatures. *Materials for Renewable and Sustainable Energy* **2018**, *7* (2), 1-7.
- 44. Ohta, H.; Kamiya, M.; Kamiya, T.; Hirano, M.; Hosono, H., UV-detector based on pn-Heterojunction Diode Composed of Transparent Oxide Semiconductors, p-NiO/n-ZnO. *Thin Solid Films* **2003**, *445* (2), 317-321.
- 45. Lee, M. J.; Seo, S.; Kim, D. C.; Ahn, S. E.; Seo, D. H.; Yoo, I. K.; Baek, I. G.; Kim, D. S.; Byun, I. S.; Kim, S. H.; Hwang, I. R.; Kim, J. S.; Jeon, S. H.; Park, B. H., A Low-

- Temperature-Grown Oxide Diode as a New Switch Element for High-Density, Nonvolatile Memories. *Adv. Mater.* **2007**, *19* (1), 73-76.
- 46. Dey, S.; Nag, S.; Santra, S.; Ray, S. K.; Guha, P. K., Voltage-controlled NiO/ZnO p—n Heterojunction Diode: a New Approach towards Selective VOC sensing. *Microsystems & Nanoengineering* **2020**, *6* (1), 35.
- 47. Ohta, H.; Orita, M.; Hirano, M.; Hosono, H., Fabrication and Characterization of Ultraviolet-emitting Diodes Composed of Transparent p-n Heterojunction, p-SrCu2O2 and n-ZnO. *Journal of Applied Physics* **2001**, *89* (10), 5720-5725.
- 48. Zhang, J.; Tanaka, H.; Kawai, T., Rectifying Characteristic in All-Perovskite Oxide Film p-n junction with Room Temperature Ferromagnetism. *Applied Physics Letters* **2002**, *80* (23), 4378-4380.
- 49. Ohta, H.; Mizoguchi, H.; Hirano, M.; Narushima, S.; Kamiya, T.; Hosono, H., Fabrication and Characterization of Heteroepitaxial p-n Junction Diode Composed of Wide-gap Oxide Semiconductors p-ZnRh2O4/n-ZnO. *Applied Physics Letters* **2003**, *82* (5), 823-825.
- 50. Tonooka, K.; Bando, H.; Aiura, Y., Photovoltaic Effect Observed in Transparent p—n Heterojunctions based on Oxide Semiconductors. *Thin Solid Films* **2003**, *445* (2), 327-331.
- 51. Ajimsha, R. S.; Vanaja, K. A.; Jayaraj, M. K.; Misra, P.; Dixit, V. K.; Kukreja, L. M., Transparent p-AgCoO2/n-ZnO Diode Heterojunction Fabricated by Pulsed Laser Deposition. *Thin Solid Films* **2007**, *515* (18), 7352-7356.
- 52. Schlupp, P.; Schein, F.-L.; von Wenckstern, H.; Grundmann, M., All Amorphous Oxide Bipolar Heterojunction Diodes from Abundant Metals. *Advanced Electronic Materials* **2015**, *1* (1-2), 1400023.
- 53. von Wenckstern, H.; Splith, D.; Lanzinger, S.; Schmidt, F.; Müller, S.; Schlupp, P.; Karsthof, R.; Grundmann, M., pn-Heterojunction Diodes with n-Type In2O3. *Advanced Electronic Materials* **2015**, *I* (4), 1400026.
- 54. Grundmann, M.; Karsthof, R.; von Wenckstern, H., Interface Recombination Current in Type II Heterostructure Bipolar Diodes. *ACS Applied Materials & Interfaces* **2014**, *6* (17), 14785-14789.
- 55. Ai, L.; Fang, G.; Yuan, L.; Liu, N.; Wang, M.; Li, C.; Zhang, Q.; Li, J.; Zhao, X., Influence of Substrate Temperature on Electrical and Optical Properties of P-type Semitransparent Conductive Nickel Oxide Thin Films Deposited by Radio Frequency Sputtering. *Applied Surface Science* **2008**, *254* (8), 2401-2405.
- 56. Vanaja, K. A.; Bhatta, U. M.; Ajimsha, R. S.; Jayalekshmi, S.; Jayaraj, M. K., p-AgCoO2/n-ZnO Heterojunction Diode grown by RF Magnetron Sputtering. *Bulletin of Materials Science* **2008**, *31* (5), 753-758.
- 57. Kim, S.; Seok, H.; Lee, H.; Lee, M.; Choi, D.; Chai, K., Fabrication of Transparent p–n Junction Diode based on Oxide Semiconductors Deposited by RF Magnetron Sputtering. *Ceram. Int.* **2012**, *38*, S623-S626.
- 58. Sanal, K. C.; Jayaraj, M. K., Growth and Characterization of Tin Oxide Thin Films and Fabrication of Transparent p-SnO/n-ZnO p—n Hetero Junction. *Materials Science and Engineering: B* **2013**, *178* (12), 816-821.

- 59. Martins, R.; Barquinha, P.; Ferreira, I.; Pereira, L.; Goncalves, G.; Fortunato, E., Role of Order and Disorder on the Electronic Performances of Oxide Semiconductor Thin Film Transistors. *Journal of Applied Physics* **2007**, *101* (4).
- 60. Lajn, A.; von Wenckstern, H.; Grundmann, M.; Wagner, G.; Barquinha, P.; Fortunato, E.; Martins, R., Comparative Study of Transparent Rectifying Contacts on Semiconducting Oxide Single Crystals and Amorphous Thin Films. *Journal of Applied Physics* **2013**, *113* (4), 044511.
- 61. Tiwari, B.; Bahubalindruni, P. G.; Santa, A.; Martins, J.; Mittal, P.; Goes, J.; Martins, R.; Fortunato, E.; Barquinha, P., Oxide TFT Rectifiers on Flexible Substrates Operating at NFC Frequency Range. *IEEE Journal of the Electron Devices Society* **2019**, *7*, 329-334.
- 62. Lorenz, M.; Lajn, A.; Frenzel, H.; v. Wenckstern, H.; Grundmann, M.; Barquinha, P.; Martins, R.; Fortunato, E., Low-temperature Processed Schottky-gated Field-effect Transistors based on Amorphous Gallium-Indium-Zinc-Oxide Thin Films. *Applied Physics Letters* **2010**, *97* (24), 243506.
- 63. Ide, K.; Nomura, K.; Hosono, H.; Kamiya, T., Electronic Defects in Amorphous Oxide Semiconductors: A Review. *physica status solidi (a)* **2019**, *216* (5), 1800372.
- 64. Hosono, H.; Ogo, Y.; Yanagi, H.; Kamiya, T., Bipolar Conduction in SnO Thin Films. *Electrochemical and Solid-State Letters* **2011**, *14* (1), H13.
- 65. Govaerts, K.; Saniz, R.; Partoens, B.; Lamoen, D., van der Waals Bonding and the Quasiparticle Band Structure of SnO from First Principles. *Physical Review B* **2013**, *87* (23), 235210.
- 66. Quackenbush, N. F.; Allen, J. P.; Scanlon, D. O.; Sallis, S.; Hewlett, J. A.; Nandur, A. S.; Chen, B.; Smith, K. E.; Weiland, C.; Fischer, D. A.; Woicik, J. C.; White, B. E.; Watson, G. W.; Piper, L. F. J., Origin of the Bipolar Doping Behavior of SnO from X-ray Spectroscopy and Density Functional Theory. *Chem. Mat.* **2013**, *25* (15), 3114-3123.
- 67. Guzmán-Caballero, D. E.; Quevedo-López, M. A.; Ramírez-Bon, R., Optical Properties of p-type SnOx Thin Films Deposited by DC Reactive Sputtering. *Journal of Materials Science: Materials in Electronics* **2019**, *30* (2), 1366-1373.
- 68. Lee, S.; Paine, D. C., On the Effect of Ti on the Stability of Amorphous Indium Zinc Oxide used in Thin Film Transistor Applications. *Applied Physics Letters* **2011**, *98* (26), 262108.
- 69. Freund, H.-J., P. K. Ghosh: Introduction to Photoelectron Spectroscopy, Vol. 67 aus: Chemical Analysis: A Series of Monographs on Analytical Chemistry and its Applications, John Wiley + Sons Ltd., New York, Chichester, Brisbane, Toronto, Singapore 1983. 377 Seiten, Preis: £ 52.25. Berichte der Bunsengesellschaft für physikalische Chemie 1984, 88 (2), 183-184.
- 70. Yu, E. T.; Croke, E. T.; Chow, D. H.; Collins, D. A.; Phillips, M. C.; McGill, T. C.; McCaldin, J. O.; Miles, R. H., Measurement of the Valence Band Offset in Novel Heterojunction Systems Si Ge (100) and AlSb ZnTe (100). *Journal of Vacuum Science & Technology B* **1990**, 8 (4), 908-915.

Table of Contents (TOC)/Abstract Graphic

<Table of Contents graphic>

